applied sciences

MDPI

Article

Proposal and Experimental Study on a Diagnosis Method for Hermetic Refrigeration Compressor Using Dual Time-Frequency Image Fusion

Kang Li [1], Zhe Sun [1], Huaqiang Jin [2,3], Yingjie Xu [1], Jiangping Gu [2,3], Yuejin Huang [1,4], Qinjian Zhang [3,5] and Xi Shen [1,3,4,*]

1 School of Mechanical Engineering, Zhejiang University of Technology, 288 Liuhe Road, Hangzhou 310023, China; 2111902073@zjut.edu.cn (K.L.); sunzhe91@zjut.edu.cn (Z.S.); xuyingjie@zjut.edu.cn (Y.X.); yjhuang3111@sina.com (Y.H.)
2 School of Education, Zhejiang University of Technology, 288 Liuhe Road, Hangzhou 310023, China; jhq@zjut.edu.cn (H.J.); gjpcf@zjut.edu.cn (J.G.)
3 Joint Laboratory of Refrigeration Compressor Reliability Evaluation, Zhejiang University of Technology, Ltd., 288 Liuhe Road, Hangzhou 310023, China; zhangqinjian@jiaxipera.com
4 School of Engineering, Zhejiang Agriculture and Forestry University, 666 Wusu Street, Hangzhou 311300, China
5 JiaXiPera Compressor Co., Ltd., 40 Baile Road, Jiaxing 314011, China
* Correspondence: sx@zjut.edu.cn

Abstract: The hermetic refrigeration compressor is the core component of the refrigeration system, failure of which will cause energy waste and reduce service life. Fault diagnosis based on vibration signal is a research hotspot. However, it is challenging to extract features of nonlinear and non-stationary vibration signals, which severely restricts the development of this method. This paper proposes a dual time-frequency images fusion method to obtain more effective features for diagnosing compressor manufacturing defects. Firstly, two time-frequency images are obtained by implementing continuous wavelet transform and Hilbert-Huang transform of the same vibration signal sample. Then, a convolutional neural network is used for image feature extraction and fusion, where the features extracted from two time-frequency images have complementarity. A data set containing six categories of typical manufacturing defects is used to verify the proposed method. The results show that the average diagnostic accuracy of the proposed method reaches 95.9%, and the proposed method has a better performance than other methods.

Keywords: manufacturing defect diagnosis; dual time-frequency images fusion; deep learning; convolutions neural network; hermetic refrigeration compressor

Citation: Li, K.; Sun, Z.; Jin, H.; Xu, Y.; Gu, J.; Huang, Y.; Zhang, Q.; Shen, X. Proposal and Experimental Study on a Diagnosis Method for Hermetic Refrigeration Compressor Using Dual Time-Frequency Image Fusion. *Appl. Sci.* **2022**, *12*, 3033. https://doi.org/10.3390/app12063033

Academic Editor: Konstantinos Diamantaras

Received: 10 October 2021
Accepted: 1 January 2022
Published: 16 March 2022

1. Introduction

Refrigerators and air conditioners, as essential household appliances, have a very high prevalence rate around the world. A total of 1.4 billion refrigerators are used, and the annual power consumption exceeds 650 TWh/year [1]. As the main body of building energy consumption, air conditioner systems account for almost half of building energy consumption and approximately 10–20% of total energy consumption [2]. Many researchers have conducted extensive studies on refrigeration [3,4] and heat pump systems [5] in order to improve the operational efficiency of refrigeration systems and reduce energy wastage. However, as the core component of refrigerators and air conditioners, hermetic refrigeration compressors directly determine the overall performance and stability of the system. For example, failure of hermetic refrigeration compressors will cause refrigeration system failure, increase noise, reduce service life and reduce COP. Breuker and Braun's [6] research showed that compressor failures are by far the costliest failure for refrigeration systems and account for 24% of the costs. Most of the faults already exist in the process of producing

equipment. Therefore, it is necessary to diagnose the hidden faults and manufacturing defects of the assembled compressor in the production inspection link. At the same time, the type of manufacturing defect of compressors can be diagnosed, and the cause of the defect can be found. Lastly, the automated production line can be optimized.

In the past, fault diagnosis of hermetic refrigeration compressors often relied on manually identifying abnormalities by touching and hearing. This method is not only wasting manpower, but also makes it difficult to ensure accuracy. To solve this issue, a large number of researchers have studied intelligent fault diagnosis methods for hermetic refrigeration compressors. Cui et al. [7] used information entropy to analyze signal characteristics and used support vector machines (SVM) to diagnosis the fault of the compressor valve. Deng et al. [8] used infrared thermal imaging and SVM classifiers to diagnose reciprocating compressors. Farzaneh-Gord et al. [9] used multiscale sample entropy and global distance for compressor fault diagnosis. These methods can effectively diagnose the type of compressor failure. However, these methods not only require a large amount of a priori knowledge and take a lot of time, but also cannot handle complex data and big data. Since 2010, with the rapid development of data-driven methods represented by deep learning, the above issues have been easily solved. Zhang et al. [10] realized compressor fault diagnosis with the help of a deep belief network and used ensemble empirical mode decomposition to denoise the original signal. Cabrera et al. [11] used long- and short-term memory networks to diagnose compressor faults and used a Bayesian network to optimize the parameters of the model. Xiao et al. [12] constructed deep convolutional neural networks (CNN) to diagnose the fault of the reciprocating compressor air valve. In this paper, CNN are introduced to automatically learn different feature information from the signal of a hermetic compressor for fault classification.

In recent years, many studies have proposed intelligent fault diagnosis methods for rotating machinery based on vibration signals. Xu et al. [13] used raw vibration signals for fault identification of the fan. Huang et al. [14] proposed a deep decoupled CNN input as the raw signal to diagnose faults. The time series does not represent the frequency characteristics and displacement variation characteristics of the raw vibration signal. Therefore, a time-frequency processing method is introduced to represent the time-domain and frequency-domain characteristics of the raw vibration signal. Yang et al. [15] used wavelet transform to extract vibration signal features and used neural networks to classify the fault of reciprocating compressors. Pichler et al. [16] used the time-frequency method for extracting features and used logistic regression and SVM to diagnose the fault of the compressor valve. Konar et al. [17] proposed a comparative analysis of the continuous wavelet transform (CWT) and the Hilbert transform while using a genetic algorithm for fault diagnosis of asynchronous motors. Verstraete et al. [18] compared the feature extraction capabilities of short-time Fourier transforms (STFT), CWT and Hilbert-Huang transform (HHT), and finally used CNN for fault diagnosis. These methods demonstrate that the time-frequency processing method has strong feature extraction capability.

The time-frequency processing method can improve the stability of the diagnosis algorithm. It is difficult to find a method with absolute advantages because different time-frequency processing methods have different advantages for the compressor vibration signals. To avoid the disadvantage that a single type of time-frequency processing method cannot express the rich information in the raw vibration signal, this paper proposes a dual time-frequency image fusion method based on convolutional neural network for compressor manufacturing defect diagnosis. This method realizes the fusion and complementation of different time-frequency information and makes full use of the image feature recognition ability of the deep neural network. The main contributions of the paper can be summarized as follows:

(1) The proposed method uses CWT and HHT for feature extraction of the same raw vibration signal, and the extracted features are complementary. The proposed method achieves richer feature extraction for a single vibration signal and ensures the accuracy of diagnosis.

(2) The proposed method constructs a dual-channel fusion convolutional neural network that can effectively learn manufacturing defect features from two time-frequency images and fuse them to realize an end-to-end diagnosis of compressor manufacturing defect based on the time-frequency image of the vibration signal.

(3) A large number of experiments verified the differences between different time-frequency processing methods and different classification models and proved the superiority of the proposed method with higher diagnostic performance and robustness.

The rest of this paper is organized as follows: Section 2 introduces the feature extraction method—dual time-frequency images fusion. Section 3 presents a diagnosis method of hermetic refrigeration compressors based on dual time-frequency images fusion. Section 4 introduces the experimental setup and data processing. Section 5 gives the experimental results and comparative study, and Section 6 concludes the paper.

2. Feature Extraction Method—Dual Time-Frequency Images Fusion

2.1. Data Preprocessing

The time-domain signal of the compressor shows less characteristic information because the coupling between the fluid flow and the mechanical structure of the hermetic refrigeration compressor causes the vibration signal to have complex characteristics. It is necessary that the vibration signal is transformed in the time-frequency domain to obtain richer feature information. Time-frequency transform methods, such as Wigner-Ville distribution (WVD) [19], short-time Fourier transform (STFT) [20], continuous wavelet transform (CWT) [18] and Hilbert-Huang transform (HHT) [21], have been widely used to extract feature from vibration signal. However, WVD and STFT are hindered by low time-frequency concentration and cross-term interference, and they also need additional expertise and prior knowledge to identify the fault features [22,23]. The most widely used methods are CWT and HHT. In the following, the principles of the two time-frequency transformations are introduced in detail.

2.1.1. Continuous Wavelet Transforms

The continuous wavelet transform (CWT) has higher time resolution and lower frequency resolution at high frequencies and has lower time resolution and higher frequency resolution at low frequencies, which exhibits multiresolution analysis characteristics. The CWT implements the wavelet transform, which is used to analyze nonperiodic signals and transient signals at different scales or resolutions. The CWT of the signal $x(t)$ is defined as:

$$W_{\varphi}(b,a) = \frac{1}{\sqrt{|a|}} \int x(t)\varphi^{*}(\frac{t-b}{a})dt \quad (1)$$

where φ^{*} represents the conjugate transpose of the mother wavelet function φ, a is a scale factor, b is the translation factor and $|a|^{1/2}$ represents the energy normalization across the different scales.

2.1.2. Hilbert-Huang Transform

The Hilbert-Huang transform (HHT) is NASA's designated name for the combination of empirical mode decomposition (EMD) [24] and Hilbert spectral analysis (HAS). The HHT analysis process is implemented in two steps: the first step uses EMD to pre-process the data, and the original data are decomposed into a set of finite intrinsic mode functions (IMF); the second step is the Hilbert transform (HT) of the decomposed IMF to obtain energy-frequency-time distribution.

The EMD decomposes any signal in the IMFs as follows: For any data sequence, $x(t)$ and m_1, the local maximum and local minimum of the raw signal, are interpolated by cubic splines to form the mean value of the upper and lower envelopes. The difference between the signal and m_1 is defined as component h_1:

$$h_1 = x(t) - m_1 \quad (2)$$

This process can be repeated k times until h_{1k} is a basic mode component:

$$h_{1k} = h_{1(k-1)} - m_{1k} \tag{3}$$

Then the first prototype component C_1 obtained from the raw data is:

$$C_1 = h_{1k} \tag{4}$$

After sorting out C_1 from the raw data:

$$r_1 = x(t) - C_1 \tag{5}$$

Since r_1 still contains information of longer period components, r_1 is still treated as new data and processed as described above. This strategy can process all subsequent remaining components r_1. The sifting process ends when the preset stoppage criterion is satisfied. The stoppage criterion can be set as follows: when the remaining component becomes smaller than a predetermined value or when the remaining component becomes a monotonic function. The EMD algorithm is based on the local characteristics of the signal, and the basic mode components and residual components are obtained by iterative screening of the local mean. It can be explained that the decomposition and reconstruction of the signal have advantages, such as reducing noise interference and eliminating data.

According to the definition of HT, the HT of real function $x(t)$ is the real-valued function, which is defined as:

$$y(t) = H(x(t)) = \frac{1}{\pi} P \int_{-\infty}^{+\infty} \frac{x(u)}{t-u} du \tag{6}$$

Here, the P indicates the principal value of the singular integral. An analytical signal was $z(t)$, consisting of $x(t)$ and $y(t)$ in the complex number of $x(t)$.

$$z(t) = x(t) + iy(t) = a(t)e^{j\theta(t)} \tag{7}$$

Here, $a(t)$ is the amplitude of the analytical signal, and $\theta(t)$ is the phase of the analytical signal.

$$a(t) = \sqrt{x(t)^2 + y(t)^2} \tag{8}$$

$$\theta(t) = \arctan(y(t)/x(t)) \tag{9}$$

Therefore, according to the definition, the instantaneous frequency expression is:

$$\omega(t) = d\theta(t)/dt \tag{10}$$

The polar coordinate expression shown in Equation (7) further emphasizes the local characteristics. It can be seen from this expression that both amplitude and phase are functions of time, and these form the basis of signal expression in the time domain.

2.2. Establishment of Dual Time-Frequency Images Fusion

According to the above part, it can be seen that the principles of the two time-frequency transformation methods are different, so the extracted features are complementary in the dual time-frequency images. To extract more features and improve the diagnosis accuracy of compressor manufacturing defects, this paper proposes a dual time-frequency image fusion method, and its structure is shown in Figure 1. The inputs of two parallel convolution and pooling layers are different time-frequency images, and the output is the one-hot label of the input image. The CNN has been successfully applied in various aspects such as image processing [25] and speech recognition [26].

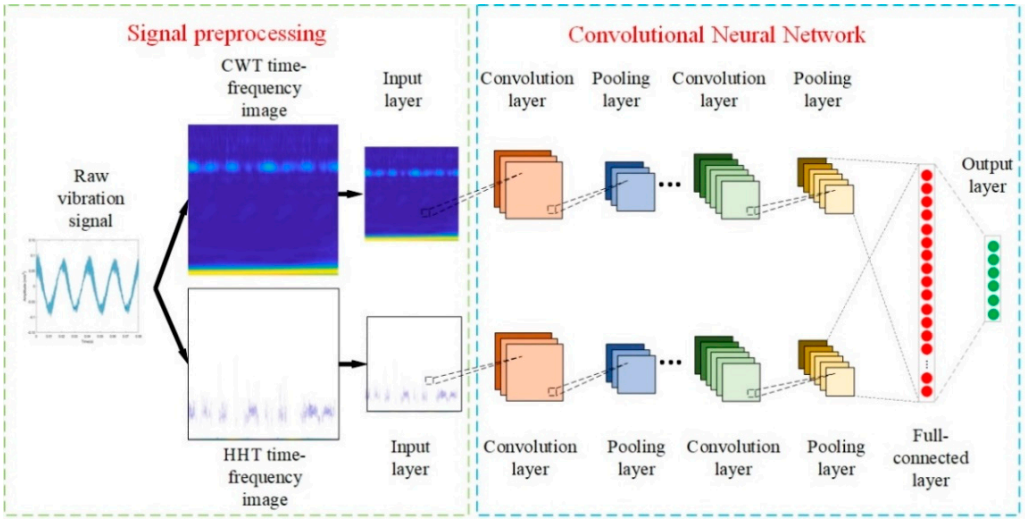

Figure 1. Structure of the proposed method.

Figure 1 shows that the proposed method structure consists of signal preprocessing and CNN. In the signal preprocessing part, CWT and HHT are performed on the same raw vibration signal to obtain two time-frequency images, which reshape to be 128 × 128 pixels. The CNN comprises two parallel convolution and pooling modules, two fully connected layers and an output layer. First, two parallel convolution and pooling modules extract features from dual time-frequency images, respectively.

Feature maps can be obtained in the convolutional layer by convolving the input images with multiple convolutional kernels. The results are input into the activation function. The formula is as follows:

$$a_{c,k} = f(X * W_{c,k} + b_{c,k}) \tag{11}$$

Here, $a_{c,k}$ represents the output of the k-th convolutional surface of the convolutional layer; $W_{c,k}$ represents the weight matrix corresponding to the k-th convolution kernel; X represents the input matrix; $b_{c,k}$ represents the bias term; and f represents the activation function. We chose the most widely used activation function ReLU.

For the pooling layer, this paper chooses the maximum pooling. The formula is as follows:

$$a_{n,k} = \max(a_{ij})i, j = 1, 2, \ldots, n \tag{12}$$

Here, $a_{n,k}$ represents the k-th pooling layer, a_{ij} represents the block of the output matrix of the previous convolutional layer and n represents the dimension of sub−block of the output matrix of the previous convolutional layer. The pooling layer often follows the convolution layers. The pooling layers play the role of quadratic feature extraction, feature dimensionality reduction and limited feature selection.

Secondly, two parallel convolution and pooling modules extract CWT time-frequency image and HHT time-frequency image features, which spliced in the first fully connected layer. Therefore, this process shows realistic feature fusion.

The calculation formula of the fully connected layer is as follows:

$$a_{fc} = f(a_n W_{fc} + b_{fc}) \tag{13}$$

Here, a_{fc} represents the output; a_n represents input; W_{fc} represents the weight matrix; b_{fc} represents the bias term; and f represents the ReLU activation function.

The fusion stage is implemented by feeding all the extracted dual time-frequency images features into a full-connected layer where the process of feature fusion is realized.

The fully connected layer passes the output value to the output layer for classification. The expression of the softmax function of the output layer is as follows:

$$\text{softmax}(y)_i = e^{y_i} \Big/ \sum_{j=1}^{n} e^{y_i} \tag{14}$$

Here, y_i represents the i-th output in the fully connected layer; $\text{softmax}(y)_i$ represents the probability of the corresponding manufacturing defect types corresponding to the i-th outputs.

The method of "Dropout" [27] is introduced within the fully connected layer to prevent over-fitting during classification. During training, some neuron in the hidden layer is stopped. This improves the network's capability to generalize and prevents overfitting.

According to the above section, the proposed method consists of four convolutional layers and pooling layers, two connected layers and a Softmax layer. We used cross-entropy loss function and Adam [28] optimization function to train the model. The learning rate is 0.001. This optimizer is suitable for models with many parameters, extensive data and small calculation memory requirements. The weights and biases of the local convolutional and fully connected layers are all trained together through backpropagation. The parameters of the proposed method are shown in Table 1, where i represents the i-th channel.

Table 1. Parameters of the proposed method.

No.	Layer Type	Kernel Size/Stride	Output Size
1	Convolution 1—i, i = 1, 2	4 × 4 × 16/1 × 1	125 × 125 × 16
2	Max-pooling 1—i, i = 1, 2	2 × 2	62 × 62 × 16
3	Convolution 2—i, i = 1, 2	4 × 4 × 32/1 × 1	59 × 59 × 32
4	Max-pooling 2—i, i = 1, 2	2 × 2	29 × 29 × 32
5	Convolution 3—i, i = 1, 2	3 × 3 × 64/1 × 1	27 × 27 × 64
6	Max-pooling 3—i, i = 1, 2	2 × 2	13 × 13 × 64
7	Convolution 4—i, i = 1, 2	3 × 3 × 128/1 × 1	13 × 13 × 128
8	Max-pooling 4—i, i = 1, 2	2 × 2	6 × 6 × 128
9	Flattened layer		1 × 15,488
10	Concatenating		1 × 30,976
11	Full-connected layer 1	128	1 × 128
12	Dropout		
13	Full-connected layer 2	32	1 × 32
14	Softmax	6	1 × 6

3. Diagnosis Method for Hermetic Refrigeration Compressor Based on Dual Time-Frequency Images Fusion

This paper proposes a dual time-frequency image fusion based on CNN to diagnose compressor manufacturing defects. This method uses CWT time-frequency image and HHT time-frequency image as the input of the CNN and automatically extracts rich features from dual time-frequency images, and extracted features are complementary. The overall framework is shown in Figure 2. The detailed procedure of the general framework is described as follows:

Step 1: Some vibration data samples are collected by accelerometers mounted on the upper surface of the compressor for different types of manufacturing defects.
Step 2: The same vibration signal is simultaneously transformed by HHT and CWT to obtain two time-frequency images.
Step 3: The time-frequency images are divided into the training set, validation set and testing set, with each group of time-frequency images being selected randomly and mapped into one−hot vectors.
Step 4: Training sets are applied to train the proposed method to obtain the optimal model parameters.

Step 5: Testing sets are input into the well−trained model for manufacturing defect diagnosis and method evaluations.

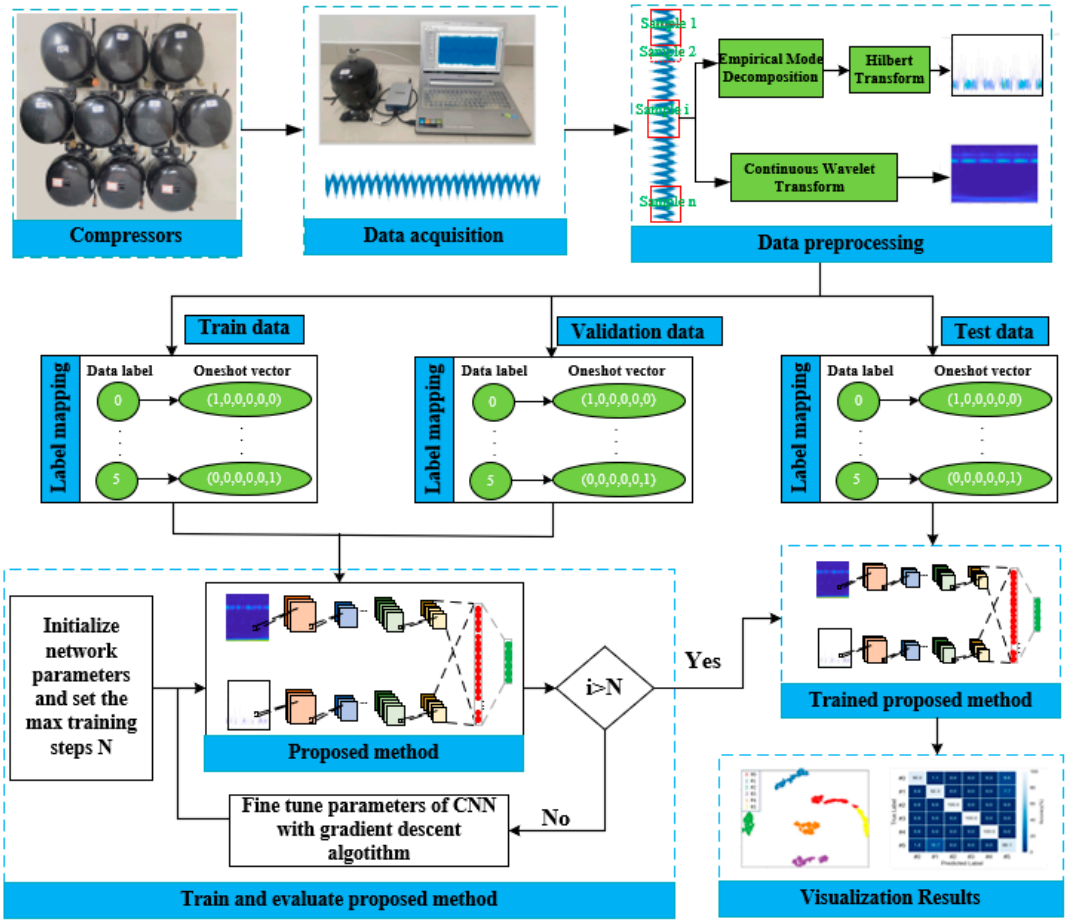

Figure 2. The overall framework of the proposed method.

4. Experimental Setup and Data Processing

4.1. Experimental Setup

The data acquisition system includes compressors, an acceleration sensor, a data acquisition card with a corresponding crate and a computer. The connectivity of the data acquisition system components is shown in Figure 3. The computer uses LabVIEW2020, a software that integrates signal measurement, control and visualization. The crate and data acquisition card are both made by National Instruments. The crate is a Cdaq-9171 minicrate, and the data acquisition card is a NI-9234 high−speed acquisition board. The acceleration sensor is installed in the center of the upper surface of the compressor, as shown in Figure 3. In order to match the detection time on the production line with the production beat, it can be seen that a sensor measuring vibration signal is the best choice. The sensor has a sensitivity of 100 mV/g. The sampling frequency of the sensor is 25.6 kHz. The speed of the compressor is 3000 rpm. These typical manufacturing defects are shown in Table 2 and Figure 4. The model is conducted in Python 3.6, 64 bits running on Windows 10 × 64, an Intel Xeon Silver 4214 CPU with 128 G and a GeForce RTX 2080Ti GPU with 11 GB. Keras version 2.1.6 is used for deep learning analysis.

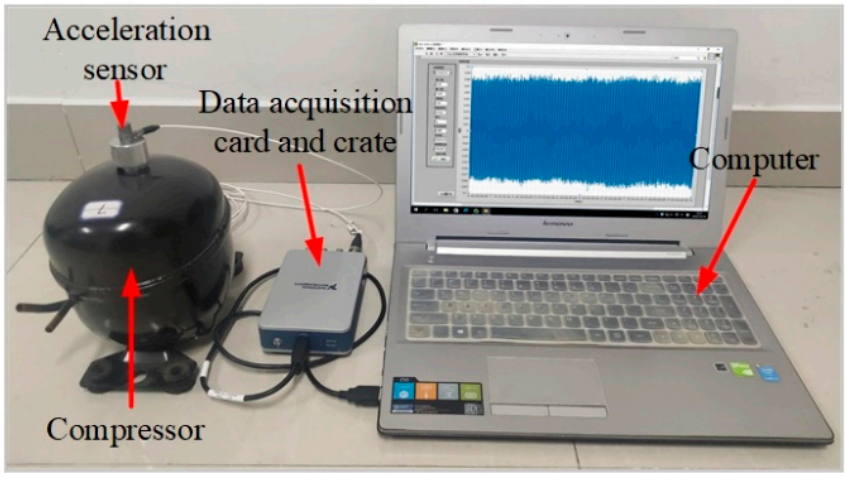

Figure 3. Experiment platform.

Table 2. Description of hermetic refrigeration compressor manufacturing defect.

Label	Manufacturing Defect Description	Number of Training/Testing Sample
#0	Normal hermetic refrigeration compressor	1200/300
#1	Discharge pipe contacting stator	1200/300
#2	Crankshaft contacting discharge pipe	1200/300
#3	Shedding of support spring	1200/300
#4	Incorrect position of silencer	1200/300
#5	Foreign body in suction valve	1200/300

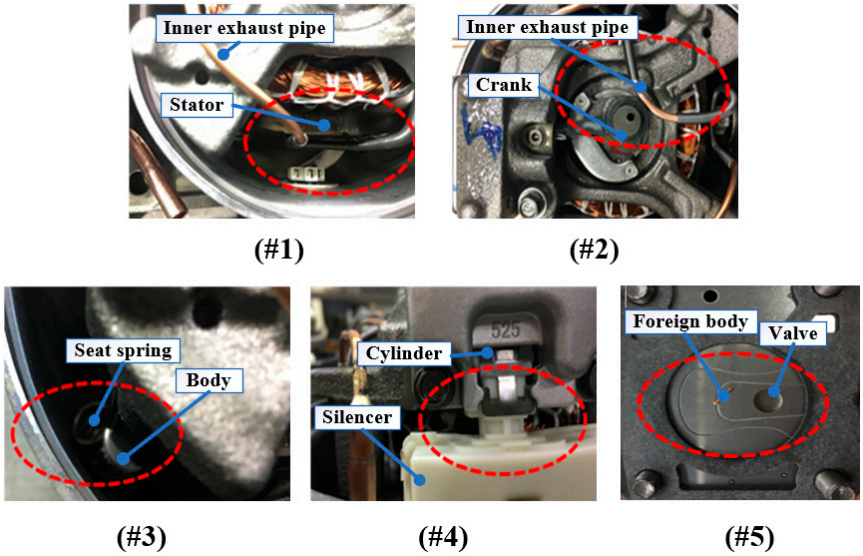

Figure 4. Fault type of hermetic refrigeration compressor. (**#1**) Discharge pipe contacting stator; (**#2**) Crankshaft contacting discharge pipe; (**#3**) Shedding of support spring; (**#4**) Incorrect position of silencer; (**#5**) Foreign body in suction valve.

In order to analyze the system of acquiring and analyzing data in energy saving, the following calculation steps are required. Firstly, we calculate the energy consumption when the acquisition and analysis system diagnoses a malfunctioning compressor. Assuming that a factory produces 3000 units a day, the probability of failure (Δ_p) is 0.5%.

$$Q_{acq} = P_{acq} * h_{acq} / (P * \Delta_p) \quad (15)$$

The power of the acquisition and analysis system (P_{acq}) is 450 w/h, and the system run time (h_{acq}) is 20 h a day. P is daily production. Therefore, Q_{acq} is 0.6 kWh.

Secondly, we calculate the energy consumption of the refrigerator when the compressor fails.

$$Q_{ref} = W_{comp} * \Delta_w * h_r * \beta \tag{16}$$

The refrigerator compressor consumes (W_{comp}) 385 kWh of energy annually [29]; the life of the refrigerator (h_r) is ten years; the utilization rate of the refrigerator (β) is 0.8; and Δ_w represents power consumed increase rate. The calculation formula of COP is as follows:

$$COP = Q_h / W \tag{17}$$

Here, Q_h represents the heating capacity (kW), and W represents the power consumed (kW).

The COP of a compressor (Δ_{cop}) reduces by about 10% when the compressor valve leaks [6]. When the heating capacity is not changed, power consumed (Δ_w) increases by about 10%.

Therefore, the energy consumption of the refrigerator increases by 308 kWh when the compressor fails. The energy that can be saved is 307.4 kWh when producing a malfunctioning compressor.

4.2. Data Processing

In the experiment, we repeated measurements 30 times for each type of manufacturing defect, and the duration of a single measure was 5 s. The total sampling time was 150 s. The sampling time of each sample was 0.1 s, and each sample contained 2560 data points. Thus, the data set had 9000 samples, of which 7200 samples are the training set, and the remaining 1800 samples are the testing set. The number of samples for the training set and test set for six typical manufacturing defects are shown in Table 2. We randomly selected 20% of the training set data as the validation set. Each sample was transformed into a group of time-frequency images using CWTs and HHTs, simultaneously. The energy scales of CWT time-frequency images and the HHT time-frequency image are [0, 0.1] and [0, 0.01], respectively.

5. Experiment Result and Comparative Study

Extensive research has been carried out to prove the superiority of the proposed method. In Section 5.1, the similarities and differences between the time-domain diagram and time-frequency image of typical manufacturing defects are introduced, proving that it is difficult to diagnose types of manufacturing defects. Section 5.2 uses confusion matrix and t-distributed stochastic neighbor embedding (t-SNE) to demonstrate the classification ability of the proposed method. In Section 5.3, four evaluation indicators are used to evaluate different diagnostic methods to illustrate the superiority of the proposed method.

5.1. Experimental Data for Typical Manufacturing Defects

Hermetic refrigeration compressors have a complex structure and many excitation sources. The raw vibration signals of six typical hermetic refrigeration compressors manufacturing defects are shown in Figure 5. It can be observed seen that the amplitude of #2 and #4 are 8 g and 0.8 g, respectively. The amplitudes of the other four typical manufacturing defect compressors are similar except for #2 and #5; the time-domain diagram of the vibration signal depicts a sine wave.

A time-frequency image is a two-dimensional data matrix that carries more information in the time and frequency domains than a one−dimensional signal. The raw vibration signals are transformed by CWT and HHT, and the time-frequency images are shown in Figures 6 and 7. Notably, the CWT time-frequency image shows more features in the low-frequency part, and the HHT time-frequency image shows more features in the high-frequency part. It can be demonstrated that the features of two time-frequency images

are complementary. It can be observed that the CWT time-frequency image has obvious frequency bands, while the HHT time-frequency image has apparent aliasing phenomena.

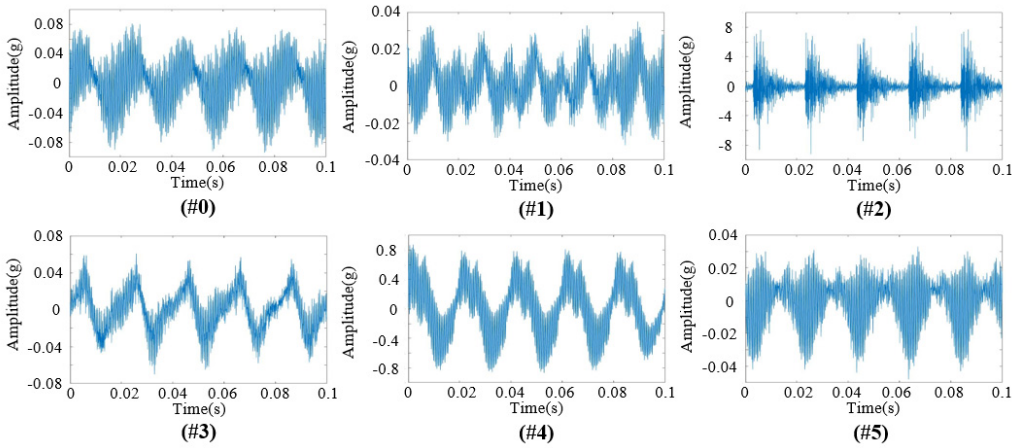

Figure 5. The time-domain diagram. (**#0**) Normal hermetic refrigeration compressor (**#1**) Discharge pipe contacting stator; (**#2**) Crankshaft contacting discharge pipe; (**#3**) Shedding of support spring; (**#4**) Incorrect position of silencer; (**#5**) Foreign body in suction valve.

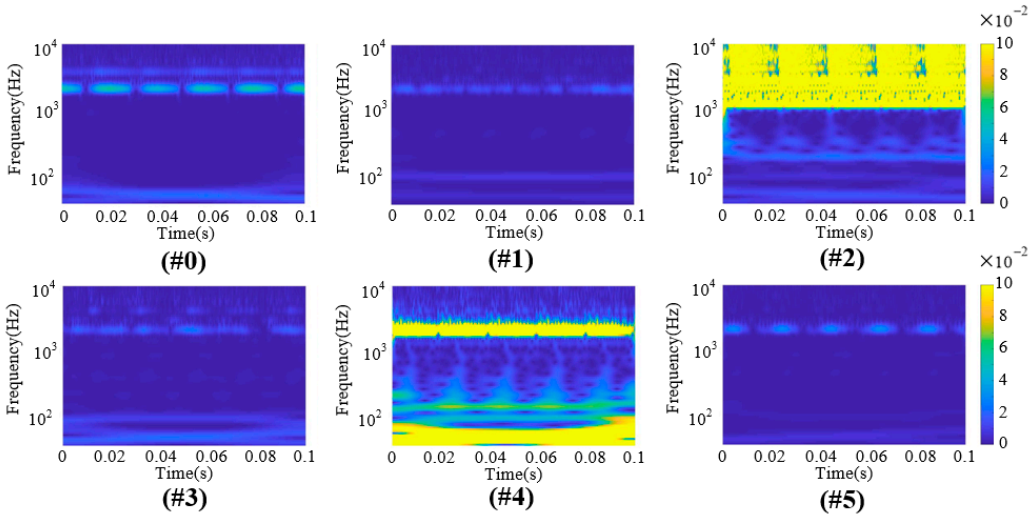

Figure 6. The CWT time-frequency image. (**#0**) Normal hermetic refrigeration compressor (**#1**) Discharge pipe contacting stator; (**#2**) Crankshaft contacting discharge pipe; (**#3**) Shedding of support spring; (**#4**) Incorrect position of silencer; (**#5**) Foreign body in suction valve.

Figures 6 and 7 show that the magnitude of the energy in the time-frequency image is proportional to the amplitude of the vibration signal. It can be seen that the time-domain diagram and the time-frequency images of some typical manufacturing defect compressors are very similar. The time-frequency characteristics of the two hermetic refrigeration compressors are different in the same type of manufacturing defect. Therefore, it is challenging to diagnose the manufacturing defects of hermetic refrigeration compressors by traditional methods.

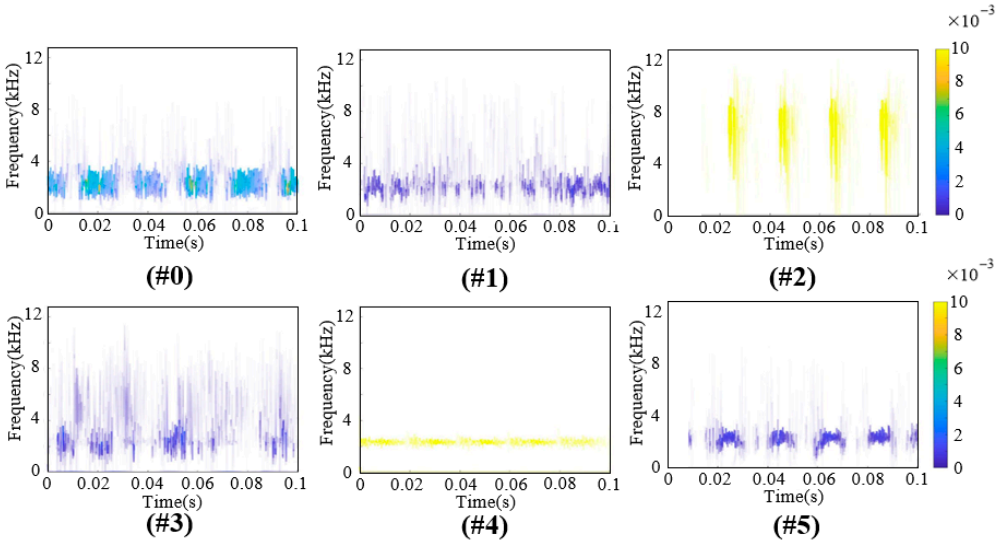

Figure 7. The HHT time-frequency image. (**#0**) Normal hermetic refrigeration compressor (**#1**) Discharge pipe contacting stator; (**#2**) Crankshaft contacting discharge pipe; (**#3**) Shedding of support spring; (**#4**) Incorrect position of silencer; (**#5**) Foreign body in suction valve.

5.2. The Performance of the Proposed Method

In this part, the performance of the proposed method is discussed for the diagnosis of each manufacturing defect. The testing set for each type of manufacturing defect has 300 samples. The testing results of the proposed method are presented by confusion matrix and t-SNE.

The confusion matrix of the proposed method is recorded ten times, and the average value is shown in Figure 8. Figure 8 clearly shows that the diagnostic accuracy of the #2, #3 and #4 are 100%; the diagnostic accuracy of the #0, #1 and #5 are 90%, 92.3% and 88.1%, respectively. It can be seen that most of the misclassified samples of #0 and #1 are diagnosed as #5, and the misclassified sample of #5 is diagnosed as #0 and #1. It can be proved that the proposed method can extract different features for classification in #2, #3 and #4. The extracted features of the proposed method are very similar in #0, #1 and #5. It can be proved that the data description of typical manufacturing defects is correct in the previous part.

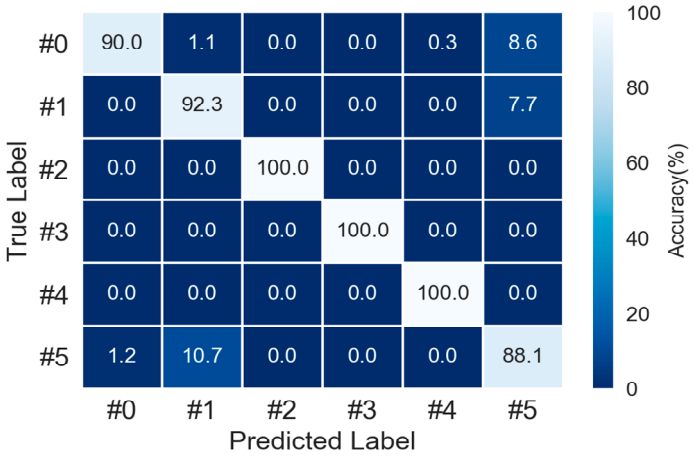

Figure 8. Confusion matrix of the proposed method.

The "t-SNE" can express the feature extraction ability of the model and analyze the clustering of features more intuitively. The visualization tool "t-SNE" implements high-dimensional feature mapping to visualize the learned characteristics, as shown in Figure 9.

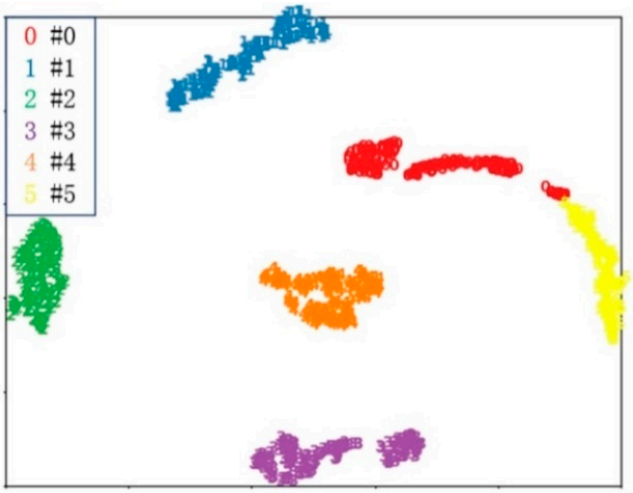

Figure 9. Visualization maps for the learned characteristics.

In Figure 9, it can be seen that the proposed model effectively learned feature information, which helps diagnose and classify a manufacturing defect, and high-level features show prominent clustering characteristics. It is concluded that the proposed method has better diagnostic performance and learned characteristics capabilities.

5.3. Comparison of Different Methods

In this part, to further illustrate that the proposed method has high diagnostic performance, the four different evaluation indexes of the proposed method are compared with those of other methods. Evaluation indicators include average *Accuracy*, *Precision*, *Recall* and *F1-score*. The formulae for average *Accuracy*, *Precision*, *Recall* and *F1-score* are (18)–(21).

$$Accuracy = \frac{|TP|+|TN|}{|TP|+|FP|+|TN|+|FN|} \tag{18}$$

$$Precision = \frac{|TP|}{|TP|+|FP|} \tag{19}$$

$$Recall = \frac{|TP|}{|TP|+|FN|} \tag{20}$$

$$F1\text{-}score = \frac{2 * Precision * Recall}{Precision + Recall} \tag{21}$$

Take #0 as an example: $|TP|$ represents the number of samples classified correctly into #0, $|TN|$ represents the number of samples classified correctly into other defects, $|FP|$ represents the number of samples classified incorrectly into #0 and $|FN|$ represents the numbers of samples in #0 classified into other classes. The *F1-score* is used to reflect the overall indicator comprehensively. Here are six different comparison methods:

(1) Artificial neural network (ANN) using raw vibration signals (RVS) as input (RVS + ANN);
(2) ANN using HHT time-frequency images as input (HHT + ANN);
(3) ANN using CWT time-frequency images as input (CWT + ANN);
(4) One−dimensional CNN using RVS as input (RVS + 1DCNN);
(5) CNN using HHT time-frequency images as input (HHT + CNN);
(6) CNN using CWT time-frequency images as input (CWT + CNN);

The input shapes and parameters of the other methods are shown in Table 3. Different methods record ten trials of diagnosis accuracy, and the average accuracy is utilized to quantify the method, as shown in Table 3. The other evaluation indicators of the different methods are shown in Figure 10 for each type of manufacturing defect.

Table 3. Comparison results of different methods.

Methods	Input Shape	Parameters	Average Accuracy	Train Time	Test Time of Each Sample
RVS + ANN	(2560, 1)	FC(N = 128, 64) + softmax(N = 6)	61.8%	26.6 s	0.0378 s
HHT + ANN	(128, 128, 3)		69.7%	186.1 s	0.0388 s
CWT + ANN	(128, 128, 3)		85.0%	188.0 s	0.0378 s
RVS + 1DCNN	(2560, 1)	C(KC = 16, 9, 9; Strides = 2, 2, 1) + P(S = 3, 3, 3) + FC(N = 128, 32) + softmax(N = 6)	69.8%	26.1 s	0.0548 s
HHT + CNN	(128, 128, 3)	C(KC = 4, 4, 3, 3; Strides = 1, 1, 1, 1) + P(S = 2, 2, 2, 2) + FC(N = 128, 32) + softmax(N = 6)	74.6%	55.8 s	0.0378 s
CWT + CNN	(128, 128, 3)		90.0%	63.3 s	0.0886 s
Proposed method	(128, 128, 3) (128, 128, 3)	—	95.9%	104.0 s	0.1314 s

C = convolution layer; P = pooling layer; FC = fully connected layers; KC = number of kernels in convolutional layer; S = subsampling rate; N = nodes.

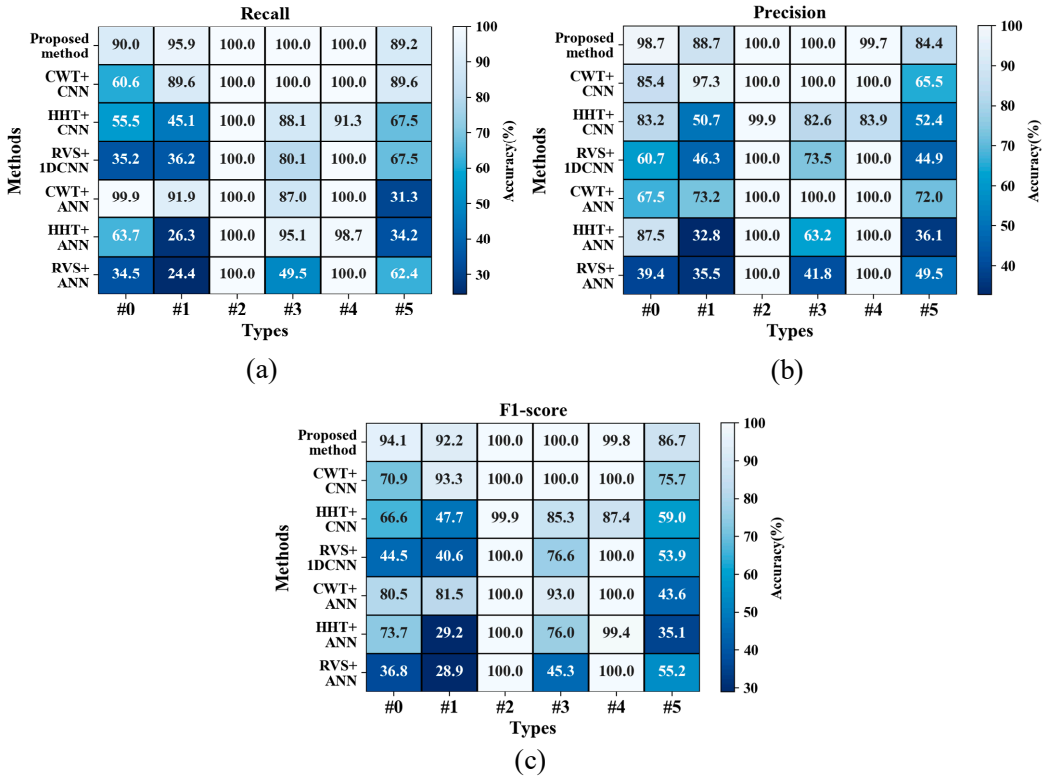

Figure 10. Performance indicators of the different methods. (**a**) Recall of different methods (**b**) Precision of different methods (**c**) F1-score of different methods.

Table 3 shows that the proposed method yields the highest accuracy up to 95.9%, training time is 104 s for 7200 samples and testing time of each sample is 0.1314 s. Therefore, it can be calculated that the proposed method can test 465 samples per minute. Comparing the diagnostic accuracy of different classifiers shows that the diagnostic accuracy of CNN is significantly higher than that of ANN. It can be explained that the CNN, as a deep model, is competent to fuse features in depth and extract more valuable features for compressor manufacturing defect diagnosis. Comparing the diagnostic accuracy of different preprocessing methods shows that the diagnostic accuracy of the HHT and CWT methods is higher than that of the RVS method because the time-frequency image can show more features than the

raw vibration signal for manufacturing defect diagnosis. The training time of the proposed method is only lower than that of the HHT + ANN method and CWT + ANN method. The testing time of each sample of the proposed method is larger than that of other methods, but the test rate meets the requirements of the production line.

Figure 10 clearly shows that the evaluation indicator of the proposed method is generally better than that of the other methods for each typical manufacturing defect. A detailed analysis of #0 shows that the recall of CWT + ANN is 9.9% higher than that of the proposed method. However, the precision of CWT + ANN is 31.2% lower than that of the proposed method in #0. From the analysis of CWT + ANN, it can be observed that a small number of normal compressor (#0) samples are misdiagnosed as other defects, but some defective compressor samples are misdiagnosed as #0. If the faulty samples are misdiagnosed as normal samples, it may lead to the failure of the refrigeration system. Thus, it is unreliable to rely only on recall and precision to evaluate the model. The F1-score is an evaluation index that combines the two indicators and comprehensively reflects the overall indicator. It can be seen from Figure 10c that the F1-score of the proposed method is 13.6% higher than that of the CWT + ANN for #0. A detailed analysis of #3 and #5 reveals that recall, precision and F1-score of the proposed method are higher than that of other methods. The recall, precision and F1-score of each typical manufacturing defect are mostly greater than 90%. It can be proved that the performance of the proposed method is superior to other methods for the diagnosis of compressor manufacturing defects. Since the dual time-frequency image features extracted can be complementary, the proposed methods obtain richer features and higher diagnostic performance.

The hermetic refrigeration compressor usually is tested in varying ambient noise levels. Therefore, it is necessary to study the diagnosis performance of the proposed methods under various conditions with a low signal-to-noise ratio (*SNR*). Robust fault diagnosis of rotating machinery is realized at low *SNR* conditions [30]. Gaussian white noise with different standard deviations is added to the raw vibration signal to create signals with different SNRs. The formula for *SNR* is given below:

$$SNR = 10\log_{10}(P_{signal}/P_{noise}) \tag{22}$$

Here, P_{signal} is the signal power, and P_{noise} is the noise power.

The diagnostic accuracy of the three models is compared when the *SNR* ranges from −6 dB to 6 dB. Each model records ten trials of diagnostic accuracy; the average diagnostic accuracy is utilized to quantify the model performance. The diagnostic accuracy of the different methods under different *SNR* is shown in Figure 11.

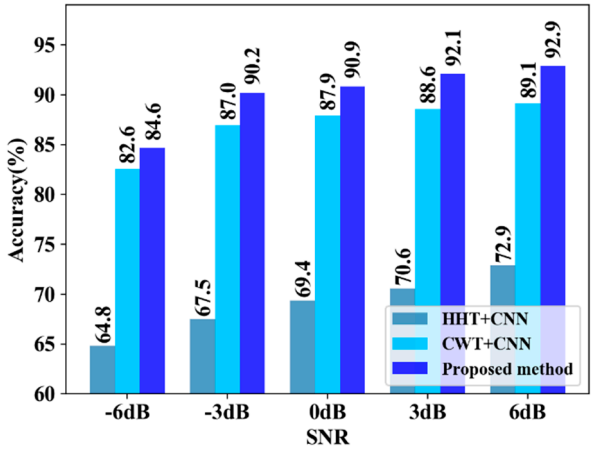

Figure 11. Accuracy of the different methods under different SNR.

It can be seen in Figure 11 that the diagnostic accuracy of different methods decreases as noise power increases. When *SNR* is 6 dB, the accuracy of the proposed method, the

CWT + CNN method and the HHT + CNN are 92.9%, 89.1% and 72.9%, respectively. When *SNR* is the same, the accuracy of the proposed method is higher than that of other methods. The result shows that the proposed method has strong antinoise abilities and robustness in noisy environments.

6. Conclusions

This paper proposes a novel diagnosis method for compressor manufacturing defects, including data processing, time-frequency feature extract using CWT and HHT and feature fusion using CNN. The main conclusions are as follows:

(1) The proposed method uses CNN to fuse the features of CWT time-frequency image and HHT time-frequency images to obtain more fault-related features for compressor manufacturing defect diagnosis.
(2) The performance of the proposed method is verified by the confusion matrix and t-SNE. The diagnostic accuracy of the proposed method is greater than 88% in each type of manufacturing defect.
(3) It is found that the average accuracy of the proposed method can reach 95.9%, which is far better than other methods. The recall, precision and F1-score of the proposed method are significantly improved for each type of manufacturing defect. Although the recall of CWT + ANN is 9.9% higher than that of the proposed method in #0, the precision and F1-score of the proposed method are 31.2% and 13.6% higher than that of CWT + ANN in #0, respectively. Therefore, this further illustrates the effectiveness of the proposed method for compressor manufacturing defect diagnosis.

The study uses vibration signals to diagnose manufacturing defects of compressors, but the diagnostic performance and the normal compressor's recall of the proposed method need to be further improved. In future work, when the diagnostic rate of the compressor matches the beat of the production line, the addition of different kinds of sensor information, such as current signal and sound signal, can be considered for integrated analysis. Adding different sensor information will improve the diagnostic performance and recall of the algorithm in different working environments.

Author Contributions: Conceptualization, K.L. and Z.S.; Methodology, K.L., H.J. and Y.H.; Software, K.L. and Z.S.; Validation, K.L., Z.S. and Y.X.; Formal analysis, K.L. and J.G.; Investigation, K.L. and H.J.; Writing—Original Draft, K.L.; Writing—Review and Editing, X.S.; Visualization, K.L. and Q.Z.; Funding acquisition, H.J. and X.S.; Supervision, Y.H. and X.S. All authors have read and agreed to the published version of the manuscript.

Funding: This work was funded by the Primary Research and Development Plan of Zhejiang Province (Grant No.2020C04010) and Zhejiang Province Public Welfare Technology Application Research Project (Grant No. LGG19E050020).

Institutional Review Board Statement: Not applicable.

Informed Consent Statement: Not applicable.

Data Availability Statement: Not applicable.

Conflicts of Interest: The authors declare no conflict of interest.

References

1. Barthel, C.; Götz, T. The overall worldwide saving potential from domestic refrigerators and freezers. *Results Detail.* **2012**, *11*, 1–5.
2. Cao, X.; Dai, X.; Liu, J. Building energy-consumption status worldwide and the state-of-the-art technologies for zero-energy buildings during the past decade. *Energy Build.* **2016**, *128*, 198–213. [CrossRef]
3. Sun, Z.; Jin, H.; Gu, J.; Huang, Y.; Wang, X.; Yang, H.; Shen, X. Studies on the online intelligent diagnosis method of undercharging sub-health air source heat pump water heater. *Appl. Therm. Eng.* **2020**, *169*, 114957. [CrossRef]
4. Sun, Z.; Jin, H.; Gu, J.; Huang, Y.; Wang, X.; Shen, X. Gradual fault early stage diagnosis for air source heat pump system using deep learning techniques. *Int. J. Refrig.* **2019**, *107*, 63–72. [CrossRef]

5. Xu, Y.; Mao, C.; Huang, Y.; Shen, X.; Xu, X.; Chen, G. Performance evaluation and multi-objective optimization of a low-temperature CO_2 heat pump water heater based on artificial neural network and new economic analysis. *Energy* **2021**, *216*, 119232. [CrossRef]
6. Breuker, M.S.; Braun, J.E. Common faults and their impacts for rooftop air conditioners. *HVAC R Res.* **1998**, *4*, 303–318. [CrossRef]
7. Cui, H.; Zhang, L.; Kang, R.; Lan, X. Research on fault diagnosis for reciprocating compressor valve using information entropy and SVM method. *J. Loss Prev. Process Ind.* **2009**, *22*, 864–867. [CrossRef]
8. Deng, R.; Lin, Y.; Tang, W.; Gu, F.; Ball, A. Object-Based Thermal Image Segmentation for Fault Diagnosis of Reciprocating Compressors. *Sensors* **2020**, *20*, 3436. [CrossRef] [PubMed]
9. Farzaneh-Gord, M.; Khoshnazar, H. Valve fault detection for single-stage reciprocating compressors. *J. Nat. Gas Sci. Eng.* **2016**, *35*, 1239–1248. [CrossRef]
10. Zhang, Y.; Ji, J.; Ma, B. Fault diagnosis of reciprocating compressor using a novel ensemble empirical mode decomposition-convolutional deep belief network. *Measurement* **2020**, *156*, 107619. [CrossRef]
11. Cabrera, D.; Guamán, A.; Zhang, S.; Cerrada, M.; Sanchez, R.-V.; Cevallos, J.; Long, J.; Li, C. Bayesian approach and time series dimensionality reduction to LSTM-based model-building for fault diagnosis of a reciprocating compressor. *Neurocomputing* **2020**, *380*, 51–66. [CrossRef]
12. Xiao, S.; Nie, A.; Zhang, Z.; Liu, S.; Song, M.; Zhang, H. Fault Diagnosis of a Reciprocating Compressor Air Valve Based on Deep Learning. *Appl. Sci.* **2020**, *10*, 6596. [CrossRef]
13. Xu, Y.; Chen, N.; Shen, X.; Xu, L.; Pan, Z.; Pan, F. Proposal and experimental case study on building ventilating fan fault diagnosis based on cuckoo search algorithm optimized extreme learning machine. *Sustain. Energy Technol. Assess.* **2021**, *45*, 100975. [CrossRef]
14. Huang, R.; Liao, Y.; Zhang, S.; Li, W. Deep decoupling convolutional neural network for intelligent compound fault diagnosis. *IEEE Access* **2018**, *7*, 1848–1858. [CrossRef]
15. Yang, B.-S.; Hwang, W.-W.; Kim, D.-J.; Tan, A.C. Condition classification of small reciprocating compressor for refrigerators using artificial neural networks and support vector machines. *Mech. Syst. Signal Process.* **2005**, *19*, 371–390. [CrossRef]
16. Pichler, K.; Lughofer, E.; Pichler, M.; Buchegger, T.; Klement, E.P.; Huschenbett, M. Fault detection in reciprocating compressor valves under varying load conditions. *Mech. Syst. Signal Process.* **2016**, *70*, 104–119. [CrossRef]
17. Konar, P.; Chattopadhyay, P. Multi-class fault diagnosis of induction motor using Hilbert and Wavelet Transform. *Appl. Soft Comput.* **2015**, *30*, 341–352. [CrossRef]
18. Verstraete, D.; Ferrada, A.; Droguett, E.L.; Meruane, V.; Modarres, M. Deep learning enabled fault diagnosis using time-frequency image analysis of rolling element bearings. *Shock Vib.* **2017**, *2017*, 5067651. [CrossRef]
19. Zou, J.; Chen, J. A comparative study on time-frequency feature of cracked rotor by Wigner–Ville distribution and wavelet transform. *J. Sound Vib.* **2004**, *276*, 1–11. [CrossRef]
20. Feng, Z.; Liang, M.; Chu, F. Recent advances in time-frequency analysis methods for machinery fault diagnosis: A review with application examples. *Mech. Syst. Signal Process.* **2013**, *38*, 165–205. [CrossRef]
21. Huang, N.E.; Shen, Z.; Long, S.R.; Wu, M.C.; Shih, H.H.; Zheng, Q.; Yen, N.-C.; Tung, C.C.; Liu, H.H. The empirical mode decomposition and the Hilbert spectrum for nonlinear and non-stationary time series analysis. *Proc. R. Soc. Lond. Ser. A Math. Phys. Eng. Sci.* **1998**, *454*, 903–995. [CrossRef]
22. Boashash, B.; Khan, N.A.; Ben-Jabeur, T. Time-frequency features for pattern recognition using high-resolution TFDs: A tutorial review. *Digit. Signal Process.* **2015**, *40*, 1–30. [CrossRef]
23. Dhamande, L.S.; Chaudhari, M.B. Compound gear-bearing fault feature extraction using statistical features based on time-frequency method. *Measurement* **2018**, *125*, 63–77. [CrossRef]
24. Pines, D.J.; Salvino, L.W. Damage Detection Using the H ilbert–H uang Transform. *Encycl. Struct. Health Monit.* **2009**. [CrossRef]
25. LeCun, Y.; Boser, B.; Denker, J.; Henderson, D.; Howard, R.; Hubbard, W.; Jackel, L. Handwritten digit recognition with a back-propagation network. *Adv. Neural Inf. Process. Syst.* **1989**, *2*, 396–404.
26. Abdel-Hamid, O.; Mohamed, A.-r.; Jiang, H.; Deng, L.; Penn, G.; Yu, D. Convolutional neural networks for speech recognition. *IEEE/ACM Trans. Audio Speech Lang. Process.* **2014**, *22*, 1533–1545. [CrossRef]
27. Srivastava, N.; Hinton, G.; Krizhevsky, A.; Sutskever, I.; Salakhutdinov, R. Dropout: A simple way to prevent neural networks from overfitting. *J. Mach. Learn. Res.* **2014**, *15*, 1929–1958.
28. Kingma, D.P.; Ba, J. Adam: A method for stochastic optimization. *arXiv* **2014**, arXiv:1412.6980.
29. Gürel, A.E.; Ağbulut, Ü.; Ergün, A.; Ceylan, İ. Environmental and economic assessment of a low energy consumption household refrigerator. *Eng. Sci. Technol. Int. J.* **2020**, *23*, 365–372. [CrossRef]
30. Ferracuti, F.; Freddi, A.; Monteriù, A.; Romeo, L. Fault Diagnosis of Rotating Machinery Based on Wasserstein Distance and Feature Selection. *IEEE Trans. Autom. Sci. Eng.* **2021**, 1–11. [CrossRef]